Current Applied Physics 25 (2021) 1–11

Contents lists available at ScienceDirect

Current Applied Physics

journal homepage: www.elsevier.com/locate/cap

Wetting layer and size effects on the nonlinear optical properties of semi oblate and prolate $Si_{0.7}Ge_{0.3}/Si$ quantum dots

M. Kria [a], Varsha [b,c], M. Farkous [a,d], V. Prasad [e], F. Dujardin [f], L.M. Pérez [g,*], D. Laroze [g], E. Feddi [a,**]

[a] Group of Optoelectronic of Semiconductors and Nanomaterials, ENSAM, Mohammed V University in Rabat, Morocco
[b] Department of Physics and Astrophysics, University of Delhi, Delhi, 110007, India
[c] Department of Physics, Kalindi College, University of Delhi, 110008, India
[d] Laboratoire des Systemes Electriques et Telcommunications, Universite Ibn Tofail, Kenitra, Morocco
[e] Department of Physics, Swami Shraddhanand College, University of Delhi, Delhi, 110036, India
[f] LCP-A2MC, Université de Lorraine, Metz, France
[g] Instituto de Alta Investigación, CEDENNA, Universidad de Tarapacá, Casilla 7 D, Arica, Chile

ARTICLE INFO

Keywords:
SiGe/Si quantum dots
Finite element simulations
Optical properties

ABSTRACT

Semi oblate and semi prolate are among the most probable self-organized nanostructures shapes. The optoelectronic properties of such nanostructures are not just manipulated with the height and lateral size but also with the wetting layer element. The practical interest of derivatives of germanium and silicon has a great important role in optoelectronic devices. This study is a contribution to the analysis of linear and nonlinear optical properties of $Si_{0.7}Ge_{0.3}/Si$. In the framework of the effective mass approximation, we solve numerically the Schrödinger equation relative to one particle confined in $Si_{0.7}Ge_{0.3}/Si$ semi prolate and semi oblate quantum dots by using the finite element method and by taking into consideration the effect of the wetting layer. The energy spectrum of the lowest states and the dipolar matrix for the fourth allowed transitions are determined and discussed. We also calculate the detailed optical properties, including absorption coefficients, refractive index changes, second and third harmonic generation as a function of the quantum dot sizes. We found that with the change in the size of prolate and oblate quantum dots, there is a shift in the resonance peaks for the absorption coefficient and refractive index. It is due to the modification in the energy levels with changing size. The study proves a redshift in the second harmonic generation and third harmonic generation coefficients with an increase in the height/radius of the oblate/prolate quantum dot, respectively. We also demonstrated the variation of wavefunction inside the quantum dot with the change in wetting layer thickness.

1. Introduction

Due to their promising optical and electronic properties, quantum dots (QDs), also labeled as artificial atoms, have attracted notable attention from theorists and experimenters [1,2]. These nanostructures are widely used in several optoelectronic devices in different fields space (LEDs, Lasers, quantum information, biomarkers, among others) [3–6]. In QDs, the quantum effects induced by both size and shape alter the energy spectra of charge carriers and control their optical and electronic properties. Thus, the choice of confinement and geometrical factors are crucial tools to design the most attractive optoelectronic devices [7,8]. The control of QD's optoelectronic properties known as bandgap engineering is supported by advancements in nanofabrication techniques that allow the design of different types of nanostructures of different shapes [9–12]. Historically, *Si*, *Ge* and their combinations $Si_{1-\eta}Ge_{\eta}$ (where η is the concentration of *Ge*) have a special place in the field of semiconductor devices and applied physics [13]. Various components demonstrate the importance of *SiGe* material in field effect transistor (FET) applications [14], complementary metal-oxide-semiconductor (CMOS), quantum well MOSFET [15], heterojunction bipolar transistor (HBT) [16], photodetectors and modulators [17,18] and tunneling devices [19,20]. The *SiGe* alloy is known for its high density, superior

* Corresponding author.
** Corresponding author.
E-mail addresses: lperez@uta.cl (L.M. Pérez), e.feddi@um5s.net.ma (E. Feddi).

https://doi.org/10.1016/j.cap.2021.02.004
Received 2 December 2020; Received in revised form 2 February 2021; Accepted 8 February 2021
Available online 23 February 2021
1567-1739/© 2021 Korean Physical Society. Published by Elsevier B.V. All rights reserved.

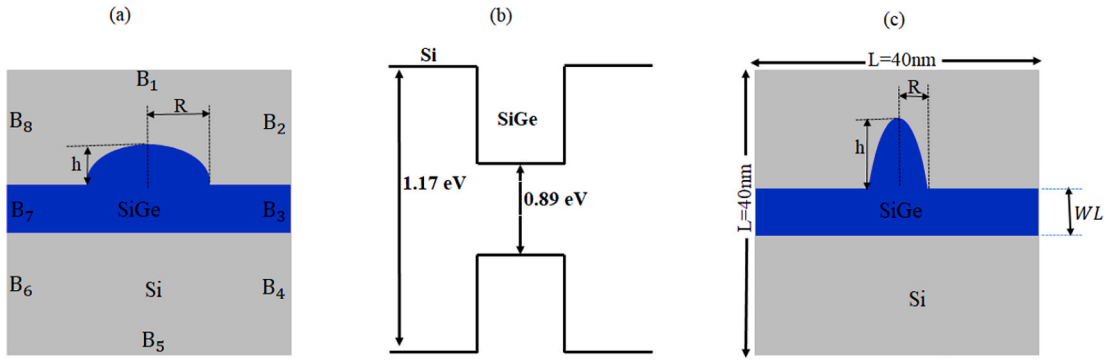


Fig. 1. (a) 2D presentation of oblate QD. (b) Energy band diagram of QD. (c) 2D presentation of prolate QD. Here h, R, and WL indicate the height, radius, and wetting layer thickness, respectively.

$$-\frac{\hbar^2}{2}\nabla\left[\frac{1}{m_i^*(r)}\nabla\psi(r)\right]+V_w^e(r)\psi(r)=E\psi(r), \tag{1}$$

optical properties, and higher dielectric constant compared to *Si* or *Ge* alone. For more details about its enormous applications, we refer the reader to some theoretical and experimental works [21–24].

It is worth mentioning that from the experimental point of view, during the growth of the *SiGe* material, QDs arise at the wetting layer. Thus, the well-known growth techniques (Starsky Kratsanov or Metalo-Organic Chemical Vapor Deposition) lead to the formation of non-homogenous islands with a large dispersion of the sizes and shapes of *SiGe* QDs [25–29]. Indeed, due to the lattices mismatch of different materials and increasing the wetting layer, the strain energy increases rapidly, and dislocated islands formation can occur to stabilize the structure. The process leads to an inhomogeneous dispersion of size and shape [25]. The forms self-organized dots tend to have different non-symmetrical shapes. The WL considered as a fine layer under the plane of QD islands has a large influence on the optoelectronic properties of QDs. To study this type of structures, authors have suggested semi-spherical, dome-shaped, lens, disk shapes [30–35]. Nevertheless, in such a growth process, we cant avoid the deformation of shape in the course of fabrication of pyramidal, prolate and oblate shapes are most acceptable are more realistic model compared to the spherical or cylindrical shapes. This consideration of shape influences the entire set of properties of these QDs.

Different methods have been used to study their optoelectronic properties. For example, Dvoyan et al. [36,37] have used the variational method to determine the impurity states in a weakly prolate and oblate ellipsoidal microcrystal under the effect of a magnetic field. They have also analyzed the optical properties as a function of the sizes, electric and magnetic fields. Dujardin *et al.* [38] studied the excitonic binding energy in prolate and oblate spheroidal QDs. Using the variational method, the authors found that the binding of the spherical case is minimal. It increases when the deformation is accentuated and explained that the bandgap is also tuned with the help of the shape of QD. Using the matrix diagonalization method, energy eigenvalues of an electron confined in ellipsoidal and semi-ellipsoidal QDs, in presence and absence of hydrogenic impurity, under an external electric field has been studied by Razaei et al. [39]. The authors have calculated the electron's low-lying states as a function of the electric field strength, the dot size, and its geometry. Baira *et al.* [40] have investigated the dome and pyramidal of *GeSn/Ge*. They have determined the optical transitions for integrated optics on *Si* substrate using the finite element method. Their study found that bigger QDs with higher aspect ratios are likely to have higher oscillator strength and longer radiative lifetime. Their results demonstrate that this QD system could be fascinating for CMOS compatible light emitters and detectors operating in the mid-*IR* range. They also evaluated the intersubband optical properties for *GeSn* pyramidal QD with the wetting layer embedded in the Ge matrix under the vertical electric field [41]. Recently, Sabaeian and Shahzadeh have developed several interesting studies concerning pyramidal and dome forms with different effects [42–45]. They have analyzed the effects of wetting layer thickness and quantum dot (QD) shape on S state and P state of strained pyramid QDs. They have demonstrated an overall redshift by increasing the WL. The same authors have analyzed the effect of size and wetting layer on subband electronic envelop functions, eigenenergies, linear and nonlinear absorption coefficients, and refractive indices of dome-shaped InAs/GaAs. They have also determined the linear, and nonlinear optical properties regarding P-to-S transition in pyramid-shaped GaAs quantum dots (QDs) coupled to wetting layer (WL) in an $Al_{0.3}Ga_{0.7}As$ matrix. Sabaeian and Riyahi [46] have investigated THz wave emission and absorption coefficients in truncated pyramidal-shaped *InAs/GaAs* quantum dots in the presence of a vertical magnetic field. Shahzadesh *et al.* [47] have analyzed the optical properties of *InAs/GaAs* oblate and semi-spheroid-shaped quantum dots coupled to WL. In this study, the perturbation method has been used combined with the exact solution for the single-band effective mass Schrödinger equation. They have shown that the electric dipole moment of the prolate QDs is more prominent with an increase in the base length than oblate QDs, with an increase in the height.

On the other hand, the nonlinear optical properties in quantum structures can be associated with the intrasubband and/or intersubband transitions. In the last years, researchers have focused on the linear and nonlinear optical properties of quantum dots: Mastering these properties requires understanding their behavior concerning the different parameters such as the size, shape, and the effect of the external medium. Many studies have treated optical non-linearity in quantum dots under different external perturbations: magnetic field, electric field, pressure, and temperature. The whole of these investigations shows that the nonlinear optical properties are susceptible to several factors: the nature of the material, the shape of the QD, and the external perturbation. It is crucial to point out that unlike the third order, the second-order response only occurs in systems that exhibit asymmetry as in the quantum medium, characterized by allowed transitions between states having the same parities. For more details we refer the reader to some interesting references [48–58]. Indeed, in these studies, the absorption coefficient, refractive index changes, second and third harmonic generations are the most investigated properties for different types of confinement: quantum wells, quantum disk, quantum wire, core/shell, conical and pyramidal dots, etc. However, to our knowledge and despite their importance, there is no study concerning the nonlinear optical properties induced by the low first state transitions of *SiGe* with the wetting layer's effect. Thus, in this study, we will try to analyze the

behavior of different optical properties: absorption coefficient, refractive index changes, second and third harmonic generation.

In the present manuscript, we focus on the lower four states and intraband transitions between these states in two configurations semi-prolate and semi-oblate QDs of $Si_{0.7}Ge_{0.3}/Si$ material and for wetting layer surrounded by *Si* matrix. It is interesting to note that the optical transitions can be controlled by the height (h) and the radius (R) of the QDs. We determine the eigenenergies, the wave functions, and the dipole matrix elements as a function of the thickness, h, and R. These results are used to analyze the linear and non-linear optical AC, RIC, SHG, and THG. The article is arranged as follows: In Section 2, we give a detailed theory and model for the system with the formulation we used, followed by detailed results and thorough discussion in Section 3. Finally, a brief conclusion is illustrated for the findings of the results in Section 4.

2. Theory and model

Let us consider semi oblate and semi prolate $Si_{0.7}Ge_{0.3}/Si$ QDs deposited on a thick SiGe wetting layer (WL) surrounded by Si matrix with dimension L^3 where $L = 40$ nm. The sketch of the system is provided in Fig. 1. The system can be described by the Schrödinger equation:where $\psi(r)$ and E are the wave function and the energy level respectively. For a given region here, the effective mass of the electron m_i^* depends on the position such that:

$$m_i^*(r) = \begin{cases} m_{SiGe}^* & \text{inside the core and the WL} \\ m_{Si}^* & \text{otherwise} \end{cases} \tag{2}$$

where $m_{Si}^* = 0.26m_0$, m_0 is the mass of free electrons. According to Fig. 1, $V_w^e(r)$ is the confining potential energy given by:

$$V_w^e(r) = \begin{cases} 0 & \text{inside the core and the WL} \\ E_g(Si) - E_g(Si_{1-\eta}Ge_\eta) & \text{otherwise} \end{cases} \tag{3}$$

where $E_g(Si) = E_g^{Si} = 1.17\ eV$. The dependence of the band gap of *SiGe* alloy on the material concentration η and temperature T is introduced by Ref. [59]:

$$E_g^{SiGe} = E_g^{Si}(1-\eta) + E_g^{Ge}\eta + C_g(1-\eta)\eta - \frac{aT^2}{b+T}, \tag{4}$$

where $E_g^{Ge} = 0.66\,eV$, $C_g = -0.4$ eV, $a = 4.73 \times 10^{-4}\ eV/K$ and $b = 636$ K. Let us recall that, for $\eta < 0.85$, the $Si_{1-\eta}Ge_\eta$ alloys are considered as Si-like material: The surfaces of equal energy are ellipsoid and the effective mass of electron can be approximated to m_{Si}^*, that is $m_{SiGe}^* \approx m_{Si}^*$.

It is important to note that given the geometrical shapes of these kinds of QDs, the analytical solution of Schrödinger equation is very complicated or even impossible. Several authors have tried to do it, but in some particular cases, such as oblate, prolate, lens, or hemispheroidal geometries. To get around this problem, we solve the Schrödinger equation by finite element method, respecting the boundary conditions defined by the problem's physical conditions and choosing an adequate method. We will return to our numerical approach in the next section. Let us also recall the electric dipolar absorption theory's main results corresponding to a transition from the ground state to the first excited state because this theory is a natural extension of the well-known theory of the optical absorption of excitons [60,61]. By neglecting the influence of the temperature and restricting ourselves to one photon transition at 0 K, we determine the changes in the optical absorption coefficient $\alpha(\omega, I)$ and refractive index $n(\omega)$. In a monochromatic electromagnetic field with frequency ω, the transition probability between two states i and f is generally known as the oscillator strength given by the Fermi golden rule. The mathematical formulation for linear ($\alpha^{(1)}$) and the third-order nonlinear photo-absorption coefficient ($\alpha^{(3)}$) is derived from the density matrix approach and perturbation theory. Thus, the expression for AC writes as [62–64]:

$$\alpha(\omega, I) = \alpha^{(1)}(\omega) + \alpha^{(3)}(\omega, I), \tag{5}$$

where,

$$\alpha^{(1)}(\omega) = \omega\sqrt{\frac{\mu}{\epsilon}}\ \frac{\hbar\ \Gamma_{\rm fi}\ |M_{\rm fi}|^2\ \sigma}{(E_{\rm fi} - \hbar\omega)^2 + (\hbar\ \Gamma_{\rm fi})^2} \tag{6}$$

and

$$\alpha^{(3)}(\omega, I) = -\omega\sqrt{\frac{\mu}{\epsilon}}\left(\frac{I}{2\epsilon_0 n_r c}\right)\frac{4\sigma\hbar\Gamma_{\rm fi}M_{\rm fi}^4}{\left[(E_{\rm fi} - \hbar\omega)^2 + (\hbar\Gamma_{\rm fi})^2\right]^2} \left[1 - \frac{(M_{\rm ff} - M_{ii})^2}{4M_{\rm fi}^2}\left\{\frac{3E_{\rm fi}^2 - 4\hbar\omega E_{\rm fi} + \hbar^2\left(\omega^2 - \Gamma_{\rm fi}^2\right)}{E_{\rm fi}^2 + (\hbar\Gamma_{\rm fi})^2}\right\}\right] \tag{7}$$

$E_{\rm fi} = E_{\rm f} - E_{\rm i}$ and $M_{\rm fi} = e < \Psi_f|x|\Psi_i >$ are the energy transition and electric dipole moment between two states i and f. We recall that the parameters used above are: c for the speed of light in a vacuum, σ_s is the electron density related to the occupied volume by the relation. I is the intensity of the incident electromagnetic radiation, ω is the angular frequency of the laser radiation, μ is the permeability of the system, n_r is the relative refractive index of semiconductor, ϵ_0 is the permittivity of free space. Also, $\Gamma_{\rm fi}$ denotes the line width and also recognized as the non-diagonal matrix element defined as the inverse of the relaxation time $\tau_{\rm fi}$ and known as the relaxation rate of initial and final states. It was found that the propagation of electromagnetic radiation through a material produces changes also in the refractive index of this material. The sum of linear and non-linear third-order refractive index changes is given by:

$$\frac{\Delta n(\omega)}{n_r} = \frac{\Delta n^{(1)}(\omega)}{n_r} + \frac{\Delta n^{(3)}(\omega)}{n_r}, \tag{8}$$

where

$$\frac{\Delta n^{(1)}(\omega)}{n_r} = \frac{1}{2\epsilon_0 n_r^2}\ \frac{\sigma M_{\rm fi}^2(E_{\rm fi} - h\omega)}{(E_{\rm fi} - \hbar\omega)^2 + (\hbar\Gamma_{\rm fi})^2} \tag{9}$$

and

$$\frac{\Delta n^{(3)}(\omega, I)}{n_r} = -\frac{\mu c I\sigma M_{\rm fi}^4}{\epsilon_0 n_r^3}\frac{(E_{\rm fi} - \hbar\omega)}{\left[(E_{\rm fi} - \hbar\omega)^2 + (\hbar\Gamma_{\rm fi})^2\right]^2}\left[1 - \frac{(M_{\rm ff} - M_{ii})^2}{4M_{\rm fi}^2\left(E_{\rm fi}^2 + (\hbar\Gamma_{\rm fi})^2\right)} \times\left\{E_{\rm fi}(E_{\rm fi} - \hbar\omega) - (\hbar\Gamma_{\rm fi})^2 - (\hbar\Gamma_{\rm fi})^2\frac{(2E_{\rm fi} - \hbar\omega)}{(E_{\rm fi} - \hbar\omega)}\right\}\right] \tag{10}$$

To have a complete description of the non-linear optical response of a system excited by an electromagnetic radiation $\mathscr{E}(t) = \mathscr{E}_0 e^{j(\omega t)} + \mathscr{E}_0 e^{-j(\omega t)}$ polarized along the z-axis, we use the development of the polarization as power series of the field strength,

$$P(t) \equiv \epsilon_0\left[\chi_\omega^{(1)}\mathscr{E}(t) + \chi_\omega^{(2)}\mathscr{E}^2(t) + \chi_\omega^{(3)}\mathscr{E}^3(t) + \ldots\right], \tag{11}$$

where $\chi_\omega^{(1)}$ is the linear susceptibility while $\chi_\omega^{(2)}$ and $\chi_\omega^{(3)}$ are defined as the second and third order non-linear optical susceptibilities. The partial development of eq. (11) leads to the usual expansion:

$$P(t) = \epsilon_0\,\chi_\omega^{(1)}\mathscr{E}_0\,e^{i\omega t} + \epsilon_0\,\chi_0^{(2)}|\mathscr{E}_0|^2 + \epsilon_0\,\chi_{2\omega}^{(2)}\,e^{2i\omega t} + \epsilon_0\,\chi_\omega^{(3)}\mathscr{E}^3\,e^{i\omega t} + \epsilon_0\,\chi_{3\omega}^{(3)}\mathscr{E}^3(t)\,e^{3i\omega t} + c.c, \tag{12}$$

such that $\chi_0^{(2)}$ $\chi_{2\omega}^{(2)}$ $\chi_\omega^{(3)}$ and $\chi_{3\omega}^{(3)}$ are the optical rectification, SHG, third order and THG susceptibility respectively. The mathematical formula-

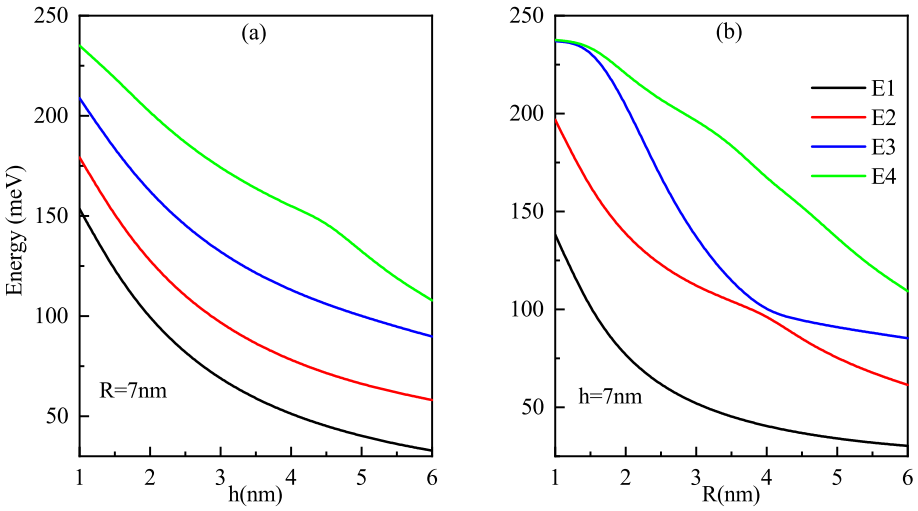


Fig. 2. Ground and excited state energies as a function of the (a) oblate QD height h with R = 7 nm and (b) prolate QD radius R with h = 7 nm.

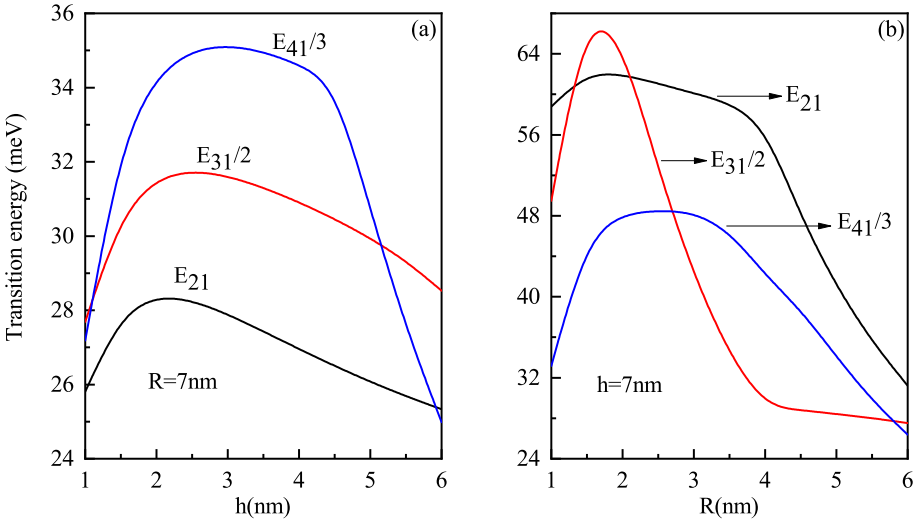


Fig. 3. Transition energies as a function of the (a) oblate QD height h with R = 7 nm and (b) prolate QD radius R with h = 7 nm.

tion of different contribution in the polarization can be deduced by using the compact density matrix method. In this study we will ignore the non-resonant terms having a non significance contribution. We will focus on the three following effects [30,65]:

$$\chi_{\omega}^{(1)} = \frac{\hbar\sigma}{\epsilon_0}\frac{|M_{21}|^2}{\hbar\omega - E_{21} - j\hbar\Gamma_{21}}, \tag{13}$$

$$\chi_{2\omega}^{(2)} = \frac{\sigma}{\epsilon_0}\frac{M_{12}M_{23}M_{31}}{(\hbar\omega - E_{21} - j\hbar\Gamma_{21})(2\hbar\omega - E_{31} - j\hbar\Gamma_{31})}, \tag{14}$$

and

$$\chi_{3\omega}^{(3)} = \frac{\sigma}{\epsilon_0}\frac{M_{12}M_{23}M_{34}M_{41}}{(\hbar\omega - E_{21} - j\hbar\Gamma_{21})(2\hbar\omega - E_{31} - j\hbar\Gamma_{31})(3\hbar\omega - E_{41} - j\hbar\Gamma_{41})}, \tag{15}$$

where interstate damping terms are as follow $\Gamma_{21} = \Gamma_{fi}$, $\Gamma_{31} = \Gamma_{fi}/2$, and $\Gamma_{41} = \Gamma_{fi}/3$. We note that the different dipolar matrix elements M_{xy} allows transitions from x to y state.

3. Results and discussion

The parameters used in the numerical calculations for $Si_{0.7}Ge_{0.3}/Si$ QD are as follows: $\sigma = 2.8 \times 10^{22} m^{-3}$, $n_r = 3.55$, $\epsilon = 13.05$, $\Gamma_{fi} = 0.38$ ps^{-1} and $I = 2 \times 10^7 W/m^2$ [66,67]. Here the width of WL is taken as 0.5 nm.

From the numerical point of view, Eq. (1) is solved with *Finite Element Method* using COMSOL Multiphysics software [68]. The Schr ödinger equation was established in the form of the general partial differential equation. As it is shown in Fig. 1a, we describe the delimitation of different regions of the structure by 8 boundaries, which are denoted by B_i with i = 1, …, 8. The eigenvalue solver was used adopting the following rules: The eigenvalues solver was used with a Neumann boundary condition $\hat{n}\cdot\nabla\psi = 0$ at (B_1, B_5), and the Dirichlet boundary condition ($\psi = 0$) at the six lateral boundaries (B_2, B_3, B_4, B_6, B_7, B_8). In addition to these conditions, we introduce the Ben-Daniel Duke continuity condition $\hat{n}\cdot(\nabla\psi/m^*_{Si_{0.7}Ge_{0.3}}) = \hat{n}\cdot(\nabla\psi/m^*_{Si})$ to take into account interface limits of Si and SiGe. We note that we used an extra refined meshing with an high degrees of nodes ~ 14400. The thickness WL was also set at 0.5 nm according to experimental reports [69].

In Fig. 2, variation of lowest four states energy with the confining parameters (h and R) is presented. We observe that for an oblate QD, (Fig. 2a), with increasing height of QD, the ground and excited states gradually decreases as the confinement is relaxed. However for prolate QD, Fig. 2b, we observe that the second excited state energy is not

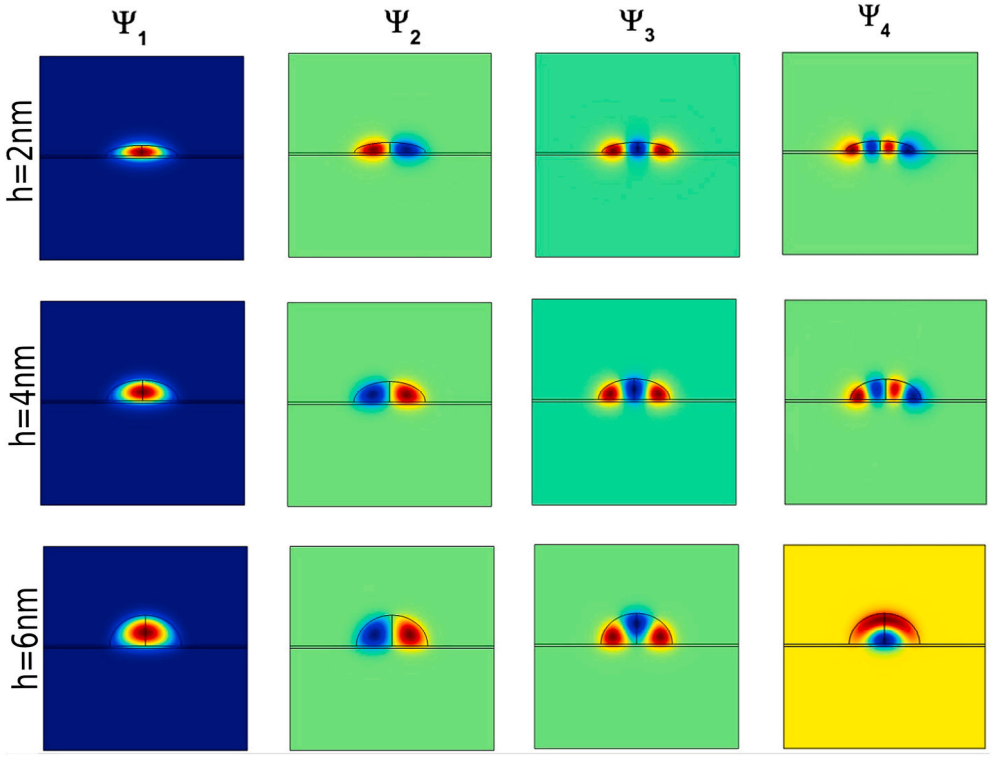


Fig. 4. The wavefunction for the four low lying states as a function of the height of the oblate QD h for a *WL thickness* = 0.5 nm and L = 40 nm.

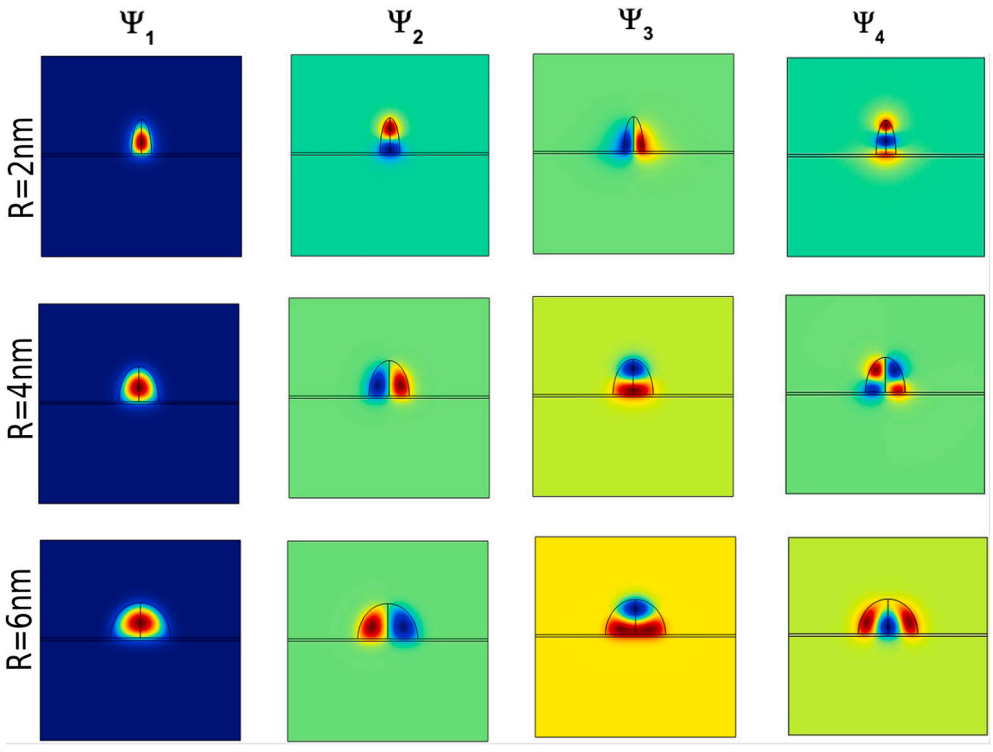


Fig. 5. The wavefunction for the four low lying states as functions of prolate QD radius R for a *WL thickness* = 0.5 nm and L = 40 nm.

decreasing with a gradual rate as compared to ground and first excited states energy with increase in radius. In both, oblate and prolate QDs with increasing size (height for oblate and radius for prolate) of QD, we notice that the third excited state energy decreases almost linearly. The behavior of all curves shows that as the confinement is relaxed (i.e as height or radius is increased), the energy of the conduction band electron decreases.

Fig. 3 shows the transition energies, E_{21}, E_{31}, and E_{41}, between the electron ground energy and the first three excited states as a function of the height h and fixed R = 7 nm in the case of the oblate QD (panel (a))

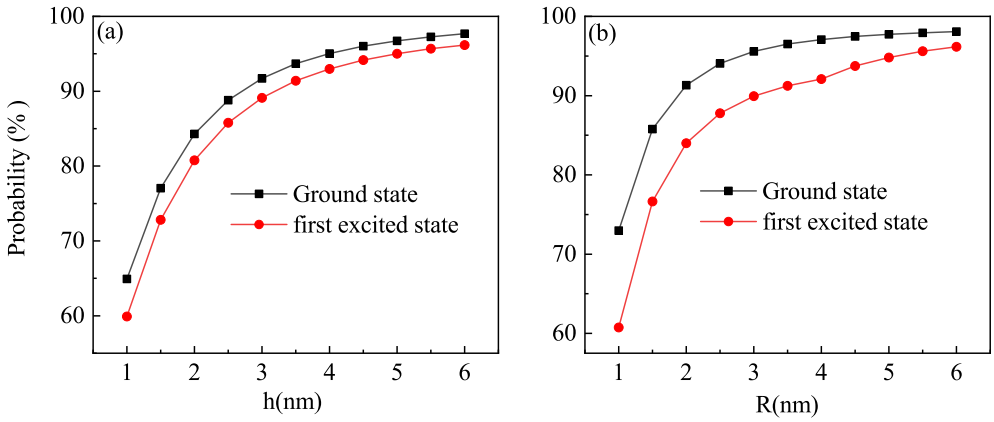


Fig. 6. Probability of finding the electron, for S-State and P-State, inside the dot region in QDs as a function of (a) oblate height *h* and (b) prolate radius *R*.

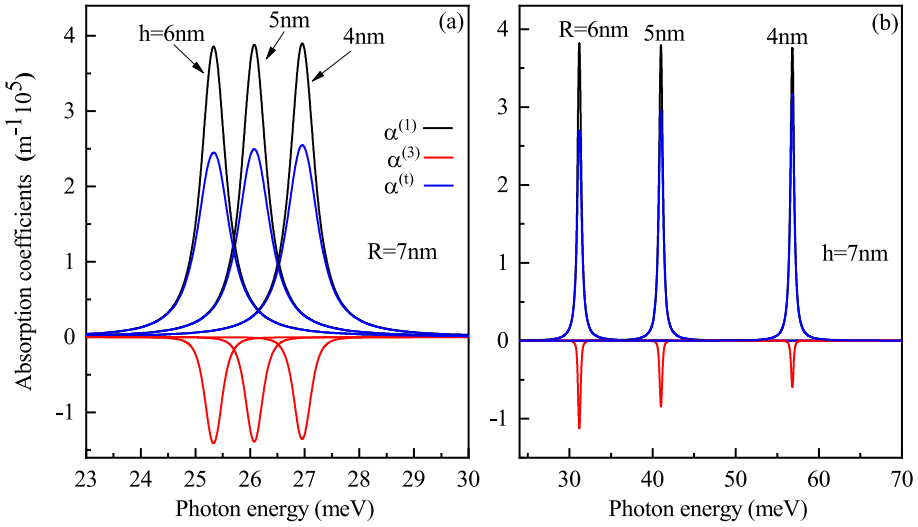


Fig. 7. Absorption coefficient as a function of the photon energy for QD (a) oblate height *h* and (b) prolate radius *R*.

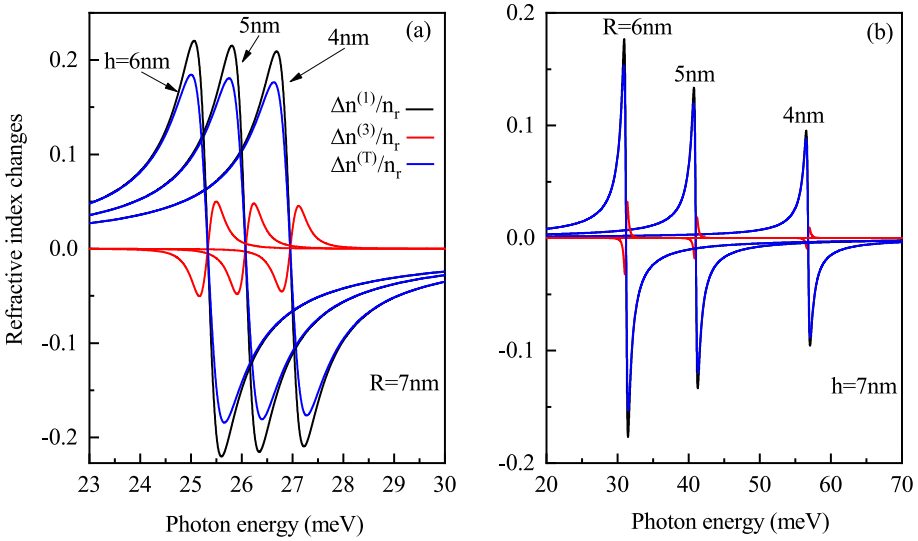


Fig. 8. Refractive index changes as a function of the photon energy for QD (a) oblate height *h* and (b) prolate radius *R*.

and as a function of radius R and a fixed h = 7 nm for prolate QD (panel (b)). Let us comment that we have limited ourselves to the first three transitions according to the detailed analysis of this process [43]. Their results conclude that only the intersubband transitions E_{12} and E_{13} are significant in the optical responses without forgetting the term E_{14} which represents the only transition between WL and the ground state

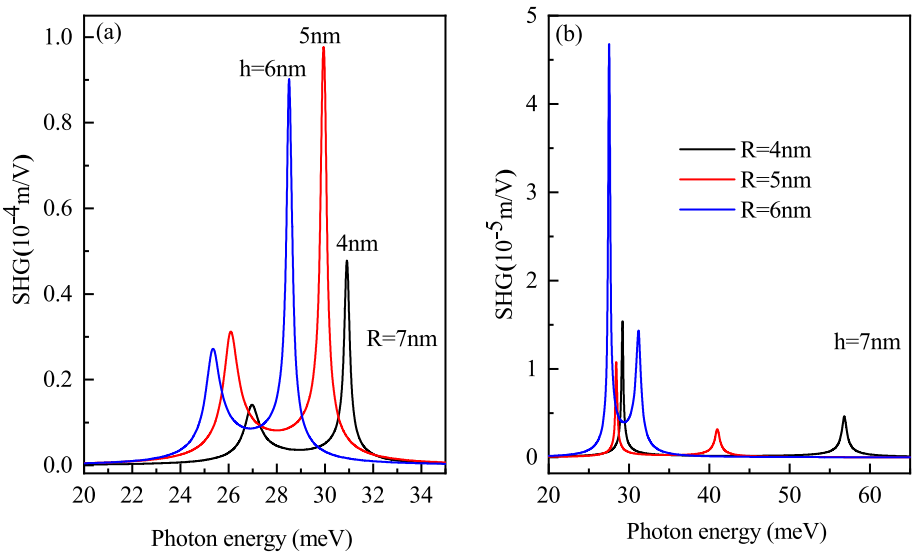


Fig. 9. Second-harmonic generation as a function of the photon energy for QD (a) oblate height *h* and (b) prolate radius *R*.

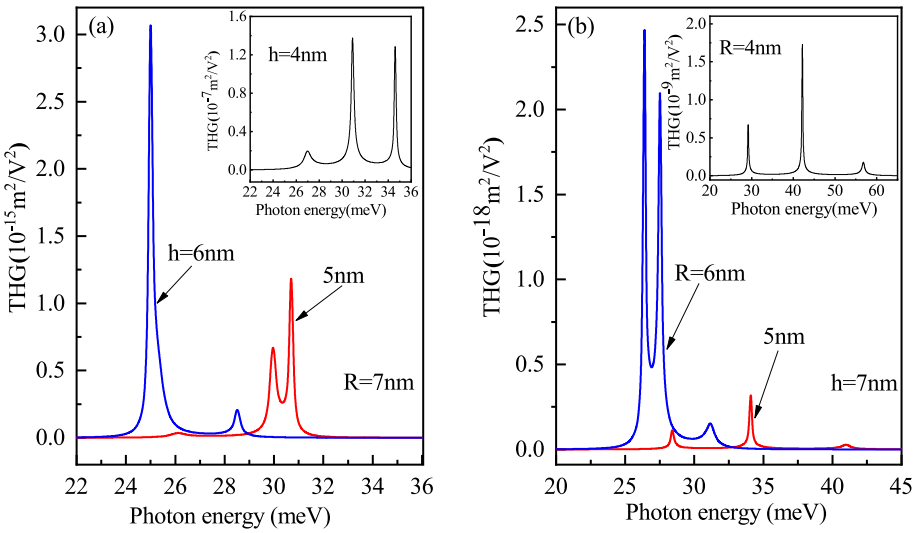


Fig. 10. Third harmonic generation as a function of the photon energy for QD (a) oblate height *h* and (b) prolate radius *R*.

which occurs in terms allowing the SHG and THG. However, the calculations are obtained for the used value of WL thickness; the third state is situated in QD. This description can be reinforced by the density representations (Fig. 4 and Fig. 5) where we can remark that the electronic clouds are situated inside the dot. The strength of confinement is falling much faster in oblate QD, where height is altering from 1 nm to 6 nm in contrast to oblate QD, where base size is changing from 1 nm to 6 nm. As can be seen from Fig. 3b, the transition energy is higher in the prolate QD case than oblate QD. This may be argued because volume change is faster in oblate QD (slow in prolate QD) as the fixed base width (height) is 7 nm. We know that the volume of semioblate/prolate QD is directly proportional to $\pi R^2 h$, so prolate QD is strongly confined compared to oblate QD, resulting in higher transition energy. These results are in good agreement with reference [38].

Figs. 4 and 5 shows the wavefunction for the ground state, first, second, and third excited state for oblate and prolate QD, respectively, for WL thickness of 0.5 nm. In Fig. 4, we observe that with an increase in the oblate QD height, the wavefunction is escalating in the four low lying states. In the ground state wavefunction, we have a single antinode, but in the first excited state wavefunction, we have two antinodes as we have both ground and first excited state available to the electron. In the second excited state wavefunction, we have three antinodes that represent the three states available for electron and four available states in the third excited state. All the antinodes are along the WL, i.e., left to right for h = 2 nm and h = 4 nm, however in the h = 6 nm case, only third excited state, the antinodes are spread along with the height of the QD. When we see the wavefunction for the prolate-shaped QD in Fig. 5, we see the change in antinode position with the change in QD size. For the ground state wavefunction, there is no change in the position of antinode with the change in the radius of prolate QD, just the wavefunction spreads more, but in the first excited state wavefunction, at R = 2 nm, we observe that the antinode is along with the height of the prolate QD whereas, for R = 4 nm and R = 6 nm case, it is along the WL. At R = 2 nm, for the second excited state wavefunction, the antinodes are along the WL of the prolate QD, and we have two antinodes, for R = 4 nm and 6 nm, the antinodes are along with the height of the prolate QD. One interesting point to note here is that for R = 4 nm, we have two antinodes, and for R = 6 nm, we still have two antinodes, but one has the tendency to split into two antinodes, which suggest that for small prolate QD, the two excited states are degenerate and in large QDs, these tend to become non-degenerate. The third excited state wavefunction is very different from the first three wavefunctions. At R = 2 nm, we have three

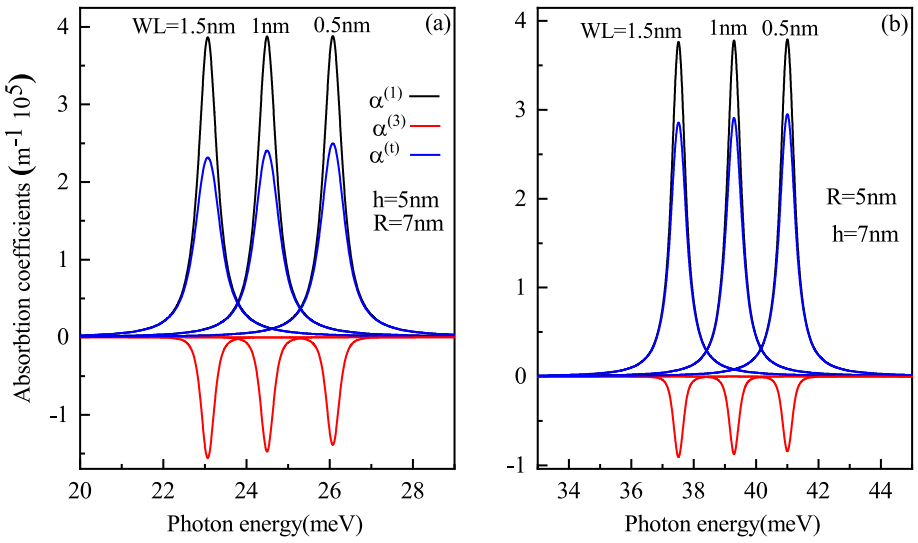


Fig. 11. Absorption coefficients as a function of the photon energy for QD (a) oblate height *h* and (b) prolate radius *R* for various wetting layer thickness. In particular, WLT = (0.5, 1.0, 1.5)nm.

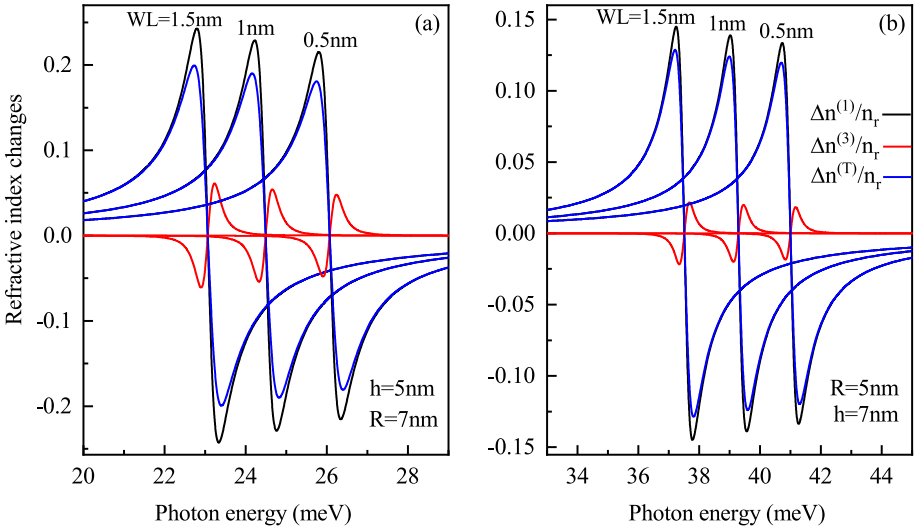


Fig. 12. Refractive index changes as a function of the photon energy for QD (a) oblate height *h* and (b) prolate radius *R* for various wetting layer thickness. In particular, WLT = (0.5, 1.0, 1.5)nm.

antinodes along with QD height, while at R = 4 nm we have four antinodes, each two lying at the same level of QD. At R = 6 nm, we have three antinodes along the WL. We observe that for this critical value of the WL thickness, the wavefunction of all the states is mainly localized in the QD.

All the antinodes are along the WL, i.e., left to right, just for h = 6 nm, the fourth low lying state antinode pattern changes. When we see the wavefunction for the prolate-shaped QD, we see the change in antinode position with the change in QD size. For the ground state wavefunction, there is no change in the position of antinode with the change in the radius of prolate QD, just the wavefunction spreads more, but in the first excited state wavefunction, at R = 2 nm, we observe that the antinode is along with the height of the prolate QD whereas, for R = 4 nm and R = 6 nm case, it is along the WL. At R = 2 nm, for the second excited state wavefunction, the antinodes are along the WL of the prolate QD, and we have two antinodes, for R = 4 nm and 6 nm, the antinodes are along with the height of the prolate QD. One interesting point to note here is that for R = 4 nm, we have two antinodes, and for R = 6 nm, we still have two antinodes, but one has the tendency to split into two antinodes, which suggest that for small prolate QD, the two excited states are degenerate and in large QDs, these tend to become non-degenerate, we observe that the electron density is confined in the WL. For h = 6 nm in oblate QD and R = 6 nm in prolate QD, the fourth low lying state has similar wavefunction. We observe that the density of electrons is more localized in the WL as compared to the QD itself in prolate shape for the second and the third excited state as two antinodes lie in the WL itself. This is why the selection of WL thickness is a crucial factor affecting the optical properties.

In Fig. 6, we present the probability of finding the electron in oblate and prolate QDs. We observe that the ground state of prolate QD has a higher probability of finding an electron in a small QD as compared to the oblate shaped QDs. It can be seen as height or radius increases the probability of finding the electron in the confined region approaches to almost 95–97.5%, i.e., with more significant h or R, the electron is certain to be found in the confined region. Of course, this also depends on the size of WL, which in this case is taken to be 0.5 nm.

Fig. 7, shows the linear, nonlinear (third-order), and total ACs for P–S state transition for both oblate and prolate QD. in Fig. 7a, we notice that

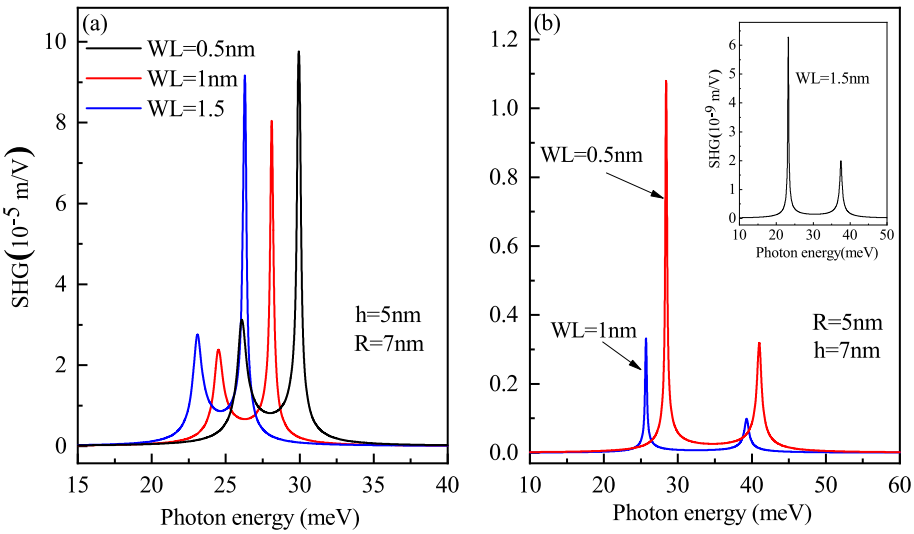


Fig. 13. Second-harmonic generation as a function of the photon energy for QD (a) oblate height *h* and (b) prolate radius *R* for various wetting layer thickness. In particular, WLT = (0.5, 1.0, 1.5)nm.

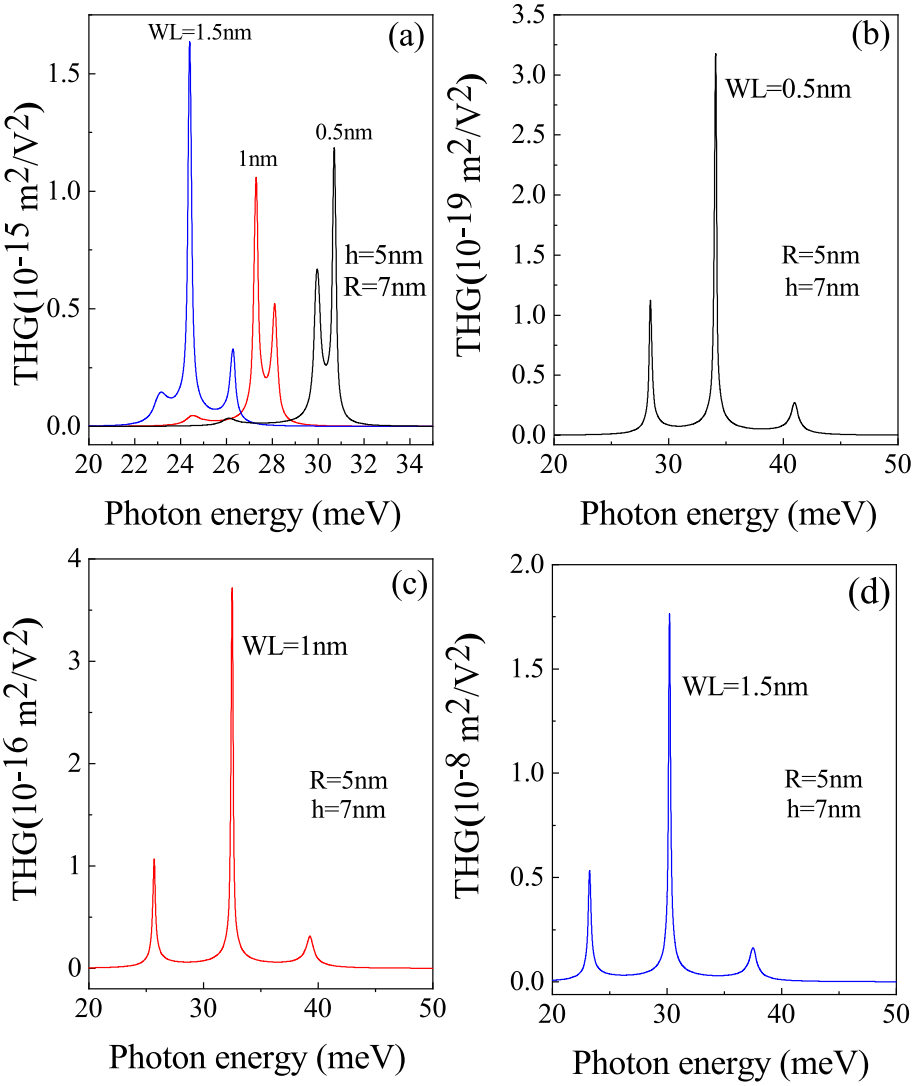


Fig. 14. Third harmonic generation as a function of the photon energy for QD (a) oblate height *h* and (b) prolate radius *R* for various wetting layer thickness. In particular, WLT = (0.5, 1.0, 1.5)nm.

the transition peak shifts towards lower photon energy with the increase in the size of the oblate QD and also the peaks are near to each other and with a gain of 1 nm in the height of oblate QD, the transition peak shifts to nearly 1 meV lower photon energy, i.e., a shift is uniform. This can be explained as the transition curve for P–S transition had a well-defined maximum peak and decrease on both sides of the peak. In Fig. 7b, here also for the increase in the radius of the prolate QD, the transition peak shifts towards the lower photon energy but here, with a gain of about 1 nm in size, the amount by which transition peak shifts is not uniform as for R = 4 nm to R = 5 nm change, the peak shifts about 20 meV to lower side of photon energy and for R = 4 nm to R = 5 nm change, the peak shifts about 10 meV to lower side of photon energy. This can be explained as the transition curve for P–S transition did not have a well defined maximum peak but instead almost a constant for a region of a radius in between 2 nm and 4nm.

Fig. 8, shows the linear, nonlinear and total refractive index changes for the corresponding transition absorption spectra in Fig. 7, absorption coefficients. As discussed for the absorption transition peaks, the same behavior is observed for the RICs curves with the increase in the size of the oblate and prolate QD. So, in the oblate QD, we can clearly see the relation of change in height and shift of the transition peak, so we can easily decide the height of oblate QD by fixing photons' energy, where we want to have our transition peak. A similar idea can be made about the prolate shaped QDs.

Fig. 9 shows the nonlinear optical coefficients of SHG as a function of the photon energy for oblate and prolate shaped QD. We notice that the prolate QD, SH peaks is ten times smaller in amplitude compared to oblate QD. Furthermore, in oblate QD, the peaks are shifting to nearly 1 meV photon energy in the left for the increase of 1 nm height of QD, whereas, in prolate QDs, with the increase in the radius of prolate QD, the coefficients of SHG peaks shows redshift as shown by oblate QD, but here the shift of peaks is not uniform as compared to oblate QD. The gap between lower and higher peak is small in oblate QD and large in prolate QD. These trends can be explained with the help of dipole matrix elements. In oblate QD, we have a uniform variation of $M_{12}M_{23}M_{31}$, but in prolate QD this factor is non-uniform.

Fig. 10 displays the nonlinear optical coefficients of THG as a function of the photon energy for oblate and prolate shaped QD. The critical point to note here is that there is a vast difference in the magnitude of harmonic peaks with the increase in the size of the QD for $\succ$4 nm for both oblate (10^{-7}) and prolate (10^{-9}) QD. Here we inspect that with the large QD, we have the redshift in coefficients of THG. On comparing our results with available results of SHG and THG coefficients in literature, we have small magnitudes of SHG and THG. The order for SHG is about $10^{-8} - 10^{-7}$ for GaAs disk-shaped QDs in the presence of spin-orbit interaction presented by Nautiyal and Silotia [70] and 10^{-16} for THG for single dopant in GaN conical QD with a spherical cap as presented by Aouami et al. [71].

To understand WL's importance in the optical response of different properties, we also obtained the figures with different WL thickness. The ACs and RICs for the ground to first excited state with three different thicknesses of WL are shown in Fig. 11 and Fig. 12 respectively for oblate (with height = 5 nm) and prolate (with radius = 5 nm) QD. In Figs. 11 and 12, we observe that with an increase in WL thickness, the absorption transition peak and RICs peak shows the redshift, and the transition peak appears at low photon energy in oblate shaped QD as compared to prolate shaped QD.

Similar results obtained in SHG and THG curves for both oblate and prolate shaped QD in Fig. 13 and Fig. 14. These results agree with the results shown in Ref. [31] for dome-shaped QD for InAs/GaAs material. This can be explained as with the increase in WL, the redshift occurs, which is the same as the increase in QD size. So, the increase of WL also enhances the volume of QDs, which results in the redshift of the peaks. Also, the shift in peaks is uniform for oblate QD and non-uniform for prolate QD.

4. Conclusion

We have studied the energy states, the transition matrix elements between different states of the oblate and the prolate shaped $Si_{0.7}Ge_{0.3}/Si$ QDs with $Si_{0.7}Ge_{0.3}$ wetting layer (WL), which is surrounded by the Si matrix. We found that the low-lying states' energy, which is important in the present study, decreases with the increasing height in oblate QD and radius in prolate QD. Also presented are the wave functions for these low lying states for both dot shapes, which present a clear picture of how antinodes change with the dots' size. The linear and non-linear absorption coefficients and the SHG, THG, and the RIC show a strong dependence size of the dots. The strain effect from lattice mismatch causes the probability of finding the electron inside the QD to vary. Finally, we understand this study will help design SiGe prolate and oblate QD based optoelectronic devices for practical applications.

Declaration of competing interest

The authors declare that they have no known competing financial interests or personal relationships that could have appeared to influence the work reported in this paper.

Acknowledgments

LMP and DL acknowledge partial financial support from FONDECYT 1180905. DL acknowledges partial financial support from Centers of Excellence with BASAL/CONICYT financing, Grant AFB180001, CEDENNA.

References

[1] D. Bimberg, M. Grundmann, N.N. Ledentsov, Quantum Dot, Heterostructures, Wiley, USA, 1999.
[2] G. Schmid, Nanoparticles: from Theory to Applications, second ed., Wiley, USA, 2010.
[3] A. Tartakovskii, Quantum Dots: Optics, Electron Transport and Future Applications, Cambridge University Press, UK, 2012.
[4] M. Mantovani, A.D. Armour, W. Belzig, G. Rastelli, Phys. Rev. B 99 (2019), 045442.
[5] P.O. Anikeeva, C.F. Madigan, J.E. Halpert, M.G. Bawendi, V. Bulović, Phys. Rev. B 78 (2008), 085434.
[6] J. Zhou, A.I. Chizhik, S. Chu, D. Jin, Nature 579 (2020) 41.
[7] M.A. Cotta, ACS Appl. Nano Mater. 6 (2020) 4920.
[8] O. Ciftja (Ed.), Quantum Dots: Applications, Synthesis and Characterization, Nova Biomedical, UK, 2012.
[9] K.L. Jahan, A. Boda, A. Chatterjee, AIP Conf. Proc. 1661 (2015), 080008.
[10] J. FlóRez, Á. Camacho, Nano. Res. Lett. 6 (2011) 268.
[11] V. Prasad, P. Silotia, Phys. Lett. A. 375 (2011) 3910.
[12] L. Shi, Z.W. Yan, Int. J. Mod. Phys. B 33 (2019) 12.
[13] S.-Y. Lee, Journal of the Korean Vacuum Society 20 (2011) 77.
[14] T.E. Whall, E.H.C. Parker, J. Appl. Phys. D. 31 (1998) 1397.
[15] D.K. Nayak, J.C. Woo, J.S. Park, K.L. Wang, K.P. MacWilliams, IEEE Electron Device Lett. EDL- 12 (1991) 154.
[16] H. Temkin, J.C. Bean, A. Antreasyan, R. Leibenguth, Appl. Phys. Lett. 52 (1988) 1089.
[17] S. Luryi, A. Kastalsky, J.C. Bean, IEEE Trans. Electron. Dev. ED-31 (1984) 1135.
[18] J.S. Park, R.P.G. Karunasiri, K.L. Wang, J. Vac. Sci. Technol. B 8 (1990) 217.
[19] S.S. Rhee, J.S. Park, R.P.G. Karunasiri, Q. Ye, K.L. Wang, Appl. Phys. Lett. 53 (1988) 204.
[20] S.S. Rhee, G.K. Chang, T.K. Carns, K.L. Wang, Appl. Phys. Lett. 56 (1990) 1061.
[21] Y.M. Haddara, P. Ashburn, D.M. Bagnall, Silicon-Germanium: Properties, Growth and Applications, Springer Handbook of Electronic and Photonic Materials, Springer International Publishing, Switzerland, 2017.
[22] S.C. Jain, W. Hayes, Semicond. Sci. Technol. 6 (1991) 547.
[23] K.L. Wang, R.P.G. Karunasiri, J. Vac. Sci. Technol. B 11 (1993) 1159.
[24] D.J. Paul, Semicond. Sci. Technol. 19 (2004) R75.
[25] M. Sabaeian, A.K. Nasab, Appl. Optic. 51 (2012) 4176.
[26] L. Seravalli, C. Bocchi, G. Trevisi, P. Frigeri, J. Appl. Phys. 108 (2010) 114313.
[27] S. Lee, O.L. Lazarenkova, P. von Allmen, F. Oyafuso, G. Klimeck, Phys. Rev. B 70 (2004) 125307.
[28] S. Sanguinetti, K. Watanabe, T. Tateno, M. Gurioli, P. Werner, M. Wakaki, N. Koguchi, J. Cryst. Growth 253 (2003) 71.
[29] S. Sanguinetti, K. Watanabe, T. Tateno, M. Wakaki, N. Koguchi, T. Kuroda, F. Minami, M. Gurioli, Appl. Phys. Lett. 81 (2002) 613.
[30] M. Shahzadeh, M. Sabaeian, AIP Adv. 4 (2014), 067134.
[31] M. Shahzadeh, M. Sabaeian, AIP Adv. 4 (2014), 067113.
[32] Y.V. Vorobiev, T.V. Torchynska, P.P. Horley, Phys. E. 51 (2013) 42.

[33] T.M. Hwang, W.W. Lin, W.C. Wang, W. Wangg, J. Comp. Physiol. 196 (2004) 208.
[34] L. Aderras, E. Feddi, A. Bah, F. Dujardin, C.A. Duque, Phys. Status Solidi (b) 254 (2017) 1700144.
[35] A. Oukerroum, E. Feddi, J. Bosch Bailach, J. Martinez-Pastor, J. Phys. Condens. Matter 22 (2010) 375301.
[36] K.G. Dvoyan, E.M. Kazaryan, Phys. Status Solidi 228 (2001) 695.
[37] K.G. Dvoyan, D.B. Hayrapetyan, E.M. Kazaryan, A.A. Tshantshapanyan, Nanoscale Res. Lett. 2 (2007) 601.
[38] F. Dujardin, E. Feddi, E. Assaid, Superlattice. Microst. 114 (2018) 296.
[39] G. Rezaei, B. Vaseghi, J. Ebrahimi, Superlattice. Microst. 49 (2011) 591.
[40] M. Baira, M. Aljaghwani, B. Salem, N.A. Madhar, B. Ilahi, Results in Phys 12 (2019) 1732.
[41] M. Baira, B. Salem, N.A. Madhar, B. Ilahi, Micromachines 10 (2019) 243.
[42] M. Sabaeian, G. Baridi, Superlattice. Microst. 144 (2020) 106582.
[43] M. Sabaeian, M. Shahzadeh, Phys. E 61 (2014) 62.
[44] M. Sabaeian, M. Shahzadeh, Phys. E 68 (2015) 215.
[45] M. Sabaeian, M. Shahzadeh, J. Appl. Phys. 116 (2014), 043102.
[46] M. Sabaeian, M. Riyahi, Phys. E 89 (2017) 105.
[47] M. Shahzadeh, M. Sabaeian, J. Opt. Soc. Am. B 32 (2015) 1097.
[48] L. Shi, Z.W. Yan, Superlattice. Microst. 94 (2016) 204.
[49] G. Rezaei, B. Vaseghi, J. Ebrahimi, Superlattice. Microst. 49 (2011) 591.
[50] R. Khordad, H. Bahramiyan, Superlattice. Microst. 76 (2014) 163.
[51] C.M. Duque, M.E. Mora-Ramos, C.A. Duque, J. Lumin. 138 (2013) 53.
[52] Varsha, P. Silotia, V. Prasad, AIP Conf. Proc 2220 (2020), 020154.
[53] Z.S. Shanon, R.S. Alnayli, K.J. Tahir, Int. J. Sci. Res. 5 (2016) 1614.
[54] S. Shao, K.X. Guo, Z.H. Zhang, N. Li, C. Peng, Solid State Commun. 151 (2011) 289.
[55] E. Kasapoglu, S. Sakiroglu, H. Sari, I. Sokmen, C.A. Duque, Heliyon. 5 (2019), e02022.
[56] I.S. Ruddock, Eur. J. Phys. 15 (1994) 53.
[57] A. El Aouami, M. Bikerouin, K. Feddi, N. Aghoutane, M. El-Yadri, E. Feddi, F. Dujardin, A. Radu, R.L. Restrepo, J.A. Vinasco, A.L. Morales, C.A. Duque, M. E. Mora-Ramos, Phil. Mag. 100 (2020) 2503.
[58] E. Paspalakis, J. Boviatsis, S. Baskoutas, J. Appl. Phys. 114 (2013) 153107.
[59] G.A. Armstrong, C.K. Maiti, Technology Computer Aided Design for Si, SiGe and GaAs Integrated Circuits, vol. **21**, IET, 2007.
[60] Y.B. Yu, H.J. Wang, Superlattice. Microst. 50 (2011) 252.
[61] R.W. Boyd, Nonlinear Optics, second ed., Academic Press, USA, 2003.
[62] M.R.K. Vahdani, G. Rezaei, Phys. Lett. A. 373 (2009) 3079.
[63] M. Kria, M. El-Yadri, N. Aghoutane, L.M. Pérez, D. Laroze, E. Feddi, Chin. J. Phys. 66 (2020) 444.
[64] M.R.K. Vahdani, G. Rezaei, Phys. Lett. A. 374 (2010) 637.
[65] M. Sabaeian, M. Shahzadeh, M. Farbod, AIP Adv. 4 (2014) 127105.
[66] M.E. Levinshtein, S.L. Rumyantsev, M.S. Shur, Properties of Advanced Semiconductor Materials: GaN,mAIN, InN, BN, SiC, SiGe, John-Wiley Sons, USA, 2001.
[67] G. Sasso, N. Rinaldi, G. Matz, C. Jungemann, Accurate mobility and energy relaxation time models for SiGe HBTs numerical simulation, in: 2009 International Conference on Simulation of Semiconductor Processes and Devices, IEEE, 2009, September, pp. 1–4.
[68] COMSOL Multiphysics software version 5.2. www.comsol.com.
[69] Y. Yu, X.-J. Shang, M.-F. Li, G.-W. Zha, J.-X. Xu, L.-J. Wang, G.-W. Wang, H.-Q. Ni, X. Dou, B. Sun, Appl. Phys. Lett. 102 (2013) 201103.
[70] V.V. Nautiyal, P. Silotia, Phys. Lett. A. 382 (2018) 2061.
[71] A. El Aouami, M. Bikerouin, K. Feddi, N. Aghoutane, M. El-Yadri, E. Feddi, F. Dujardin, A. Radu, R.L. Restrepo, J.A. Vinasco, A.L. Morales, C.A. Duque, M. E. Mora-Ramos, Phil. Mag. 100 (2020) 2503.